Time-reversal soliton pairs in even spin Chern number higher-order topological insulators

Yi-Chun Hung,[1,2,3,4] Baokai Wang,[1,4] Chen-Hsuan Hsu,[2] Arun Bansil,[1,4] and Hsin Lin[2,*]
[1]*Department of Physics, Northeastern University, Boston, Massachusetts 02115, USA*
[2]*Institute of Physics, Academia Sinica, Taipei 115201, Taiwan*
[3]*Department of Physics, National Taiwan University, Taipei 106216, Taiwan*
[4]*Quantum Materials and Sensing Institute, Northeastern University, Burlington, Massachusetts 01803, USA*

(Received 15 November 2023; revised 17 April 2024; accepted 4 June 2024; published 8 July 2024)

Solitons formed through the one-dimensional mass-kink mechanism on the edges of two-dimensional systems with nontrivial topology play an important role in the emergence of higher-order (HO) topological phases. In this connection, the existing work in time-reversal symmetric systems has focused on gapping the edge Dirac cones in the presence of particle-hole symmetry, which is not suited to the common spin Chern insulators. Here, we address the emergence of edge solitons in spin Chern number of two insulators, in which the edge Dirac cones are gapped by perturbations preserving time-reversal symmetry but breaking spin-$U(1)$ symmetry. Through the mass-kink mechanism, we thus explain the appearance of pairwise corner modes and predict the emergence of extra charges around the corners. By tracing the evolution of the mass term along the edge, we demonstrate that the in-gap corner modes and the associated extra charges can be generated through the anisotropic S_z-mixing spin-orbit coupling via the mass-kink mechanism. We thus provide strong evidence that an anisotropic even spin Chern number insulator is an HO topological insulator with protected corner charges.

DOI: 10.1103/PhysRevB.110.035125

I. INTRODUCTION

Analysis of topological properties of the ground-state electronic structures has yielded many new insights into the nature of quantum matter. The bulk-boundary correspondence not only manifests itself through the appearance of gapless edge states, but it can also lead to topological solitons and the associated topologically protected charges [1–6]. Distinct from the topological charges produced by the filling anomalies that can be predicted by bulk invariants based on symmetries [7–10], these solitons are typically generated at the interfaces that separate two regions characterized by (complex) mass terms with different phases, which we will refer to as the mass-kink mechanism in one-dimensional (1D) systems. In the low-energy states on the edges of a two-dimensional (2D) topological insulator, different phases of the massive edge Dirac cones can also induce corner solitons, indicating the presence of higher-order (HO) topological phases with protected extra corner charges [4,11–15]. In this connection, the existing literature on solitons in time-reversal-symmetric systems has focused on gapping the Dirac cones with particle-hole symmetry [16–22]. However, the role of the mass-kink mechanism in gapping Dirac cones in particle-hole symmetry-breaking systems is not well understood. Here, we examine how, in even spin Chern number insulators, the edge states can be gapped through spin-$U(1)$-symmetry-breaking terms in the Hamiltonian.

Even spin Chern number insulators have been demonstrated in several recent tight-binding models [23–25]. In the absence of S_z-mixing spin-orbit coupling (SOC), these models support insulators with a spin Chern number (C_s) of 2, which implies the presence of two spin-polarized gapless edge states protected by S_z conservation (Fig. 1). When the S_z-mixing SOC is turned on, the edge states are gapped (Fig. 2) without changing the spin Chern number [26,27]. The corner modes appear pairwise within the edge band gap in a finite-sized thin film due to time-reversal symmetry. However, the origin of these corner modes is not well understood.

Since the edge states are gapped, the nonvanishing mass terms are driven by the S_z-mixing SOC. The mass kink could thus be anticipated to account for the corner modes. Through bosonization, we will show how the corner modes and the associated corner charges can be attributed to the two time-reversal-related edge solitons via the mass-kink mechanism. These solitons form a time-reversal-related soliton pair [28] and provide an explanation of the existence of pairwise in-gap corner modes with extra charges in a finite-sized thin film. We illustrate our new approach by considering the model of Ref. [24] as a concrete example with $C_s = 2$ and S_z-mixing SOC-induced mass terms. By tracking the phase evolution of the corner modes along the edge of a thin film, we show that the corner modes and the associated extra charge arise from a time-reversal soliton pair created by the S_z-mixing SOC-induced mass-kink mechanism. These results indicate that even in the absence of gapless edge Dirac cones derived from crystalline symmetries, an HO topological insulator with protected corner charges can emerge from a $C_s = 2$ spin Chern insulator.

This paper is organized as follows. In Sec. II, we construct an effective model for the edge-hosting two Dirac cones, along with a general mass term. We show how a

*Contact author: nilnish@gmail.com

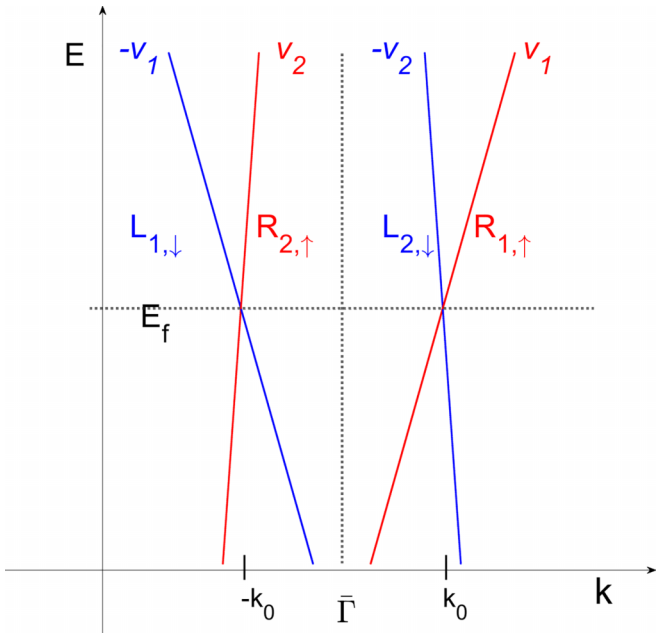

FIG. 1. A schematic diagram of our picture of the edge modes before adding the gap-opening perturbation, where the index 1(2) indicates the first(second) time-reversal sector. $R(L)$ refers to the right (left) moving mode and v is the Fermi velocity. $\pm k_0$ values of the edge Dirac cones in the edge Brillouin zone are labeled.

time-reversal-related soliton pair arises in the system, leading to an HO topological phase with corner modes. Through a renormalization group (RG) analysis, we show that our results are robust against the presence of electron-electron interaction. In Sec. III, we numerically confirm our results by considering a concrete example of a time-reversal-symmetric generalization of the Haldane model in which the mass term is induced via a S_z-mixing SOC. We summarize our results in Sec. IV. Details of the formalism in the main text are given in the Appendixes. Bosonization conventions, some basic properties, the general mass term, and the influence of intersector forward scattering are presented in Appendix A, Appendix B, Appendix C, and Appendix D, respectively.

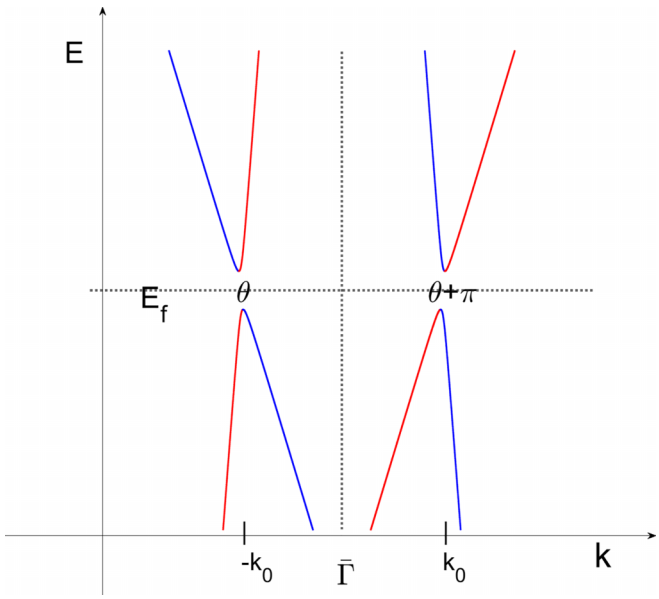

FIG. 2. A schematic diagram of our picture of the edge modes after adding the gap-opening perturbation. With the presence of time-reversal symmetry, the mass terms of different Dirac cones have a π-phase difference in their phase θ. In our case, the perturbation is the S_z-mixing SOC.

II. EDGE THEORY OF A $C_s = 2$ SPIN CHERN INSULATOR

We start by considering an edge theory of a spin Chern insulator with $C_s = 2$. Before introducing perturbations, we have two edge Dirac cones located at the momenta $\pm k_0$ with $k_0 > 0$ at the Fermi level due to the nonvanishing spin Chern number, see Fig. 1. Due to the helical nature of the edge states, the right-moving modes are locked with spin up while the left-moving modes lock with spin down (Fig. 1). Unlike systems with a single Dirac cone at a time-reversal invariant momentum, here the Dirac cones do not involve time-reversal partners. Rather, they emerge from the right-moving or the left-moving modes derived from distinct time-reversal sectors. Therefore, there is no Kramers' degeneracy in our low-energy theory. Since different time-reversal sectors can have different Fermi velocities, the Dirac cones are slightly tilted (Fig. 1).

Following the strategy used in the literature [11,29,30], we map our edges around a corner into a 1D system in which the corner is at $x = 0$ connecting two edges represented by $x > 0$ and $x < 0$ regions. We write the edge-theory model shown in Fig. 1 in real space as:

$$H_0(x) = -iv_1(R_1^\dagger \partial_x R_1 - L_1^\dagger \partial_x L_1) - iv_2(R_2^\dagger \partial_x R_2 - L_2^\dagger \partial_x L_2), \quad (1)$$

where $v_{1(2)}$ is the Fermi velocity for the first (second) time-reversal sector. We then define the average Fermi velocity $v = \frac{v_1+v_2}{2}$ and its deviation between the two time-reversal sectors $\delta v = \frac{v_2-v_1}{2}$. Eq. (1) then becomes:

$$H_0(x) = -iv\sum_{\mu=1}^{2}(R_\mu^\dagger \partial_x R_\mu - L_\mu^\dagger \partial_x L_\mu) - i\delta v\sum_{\mu=1}^{2}\epsilon^{\mu\nu}(R_\nu^\dagger \partial_x R_\nu - L_\nu^\dagger \partial_x L_\nu), \quad (2)$$

which can be further bosonized, with the convention in Appendix A, into [29]:

$$H_0^{(B)}(x) = \frac{1}{2}\sum_{\mu=1}^{2} v[(\partial_x\varphi_\mu)^2 + (\partial_x\vartheta_\mu)^2] + \frac{1}{2}\sum_{\mu=1}^{2}\delta v\epsilon^{\mu\nu}[(\partial_x\varphi_\nu)^2 + (\partial_x\vartheta_\nu)^2], \quad (3)$$

which can be further written as:

$$H_0^{(B)}(x) = \frac{v}{2}\{[(\partial_x\varphi_c)^2 + (\partial_x\vartheta_c)^2 + (\partial_x\varphi_d)^2 + (\partial_x\vartheta_d)^2] - 2\frac{\delta v}{v}[\partial_x\varphi_c\partial_x\varphi_d + \partial_x\vartheta_c\partial_x\vartheta_d]\}. \quad (4)$$

Upon adding perturbations that break the spin rotational symmetry but preserve the time-reversal symmetry, the Dirac

points can be gapped, and the low-energy theory acquires a mass term, which we introduce next.

A. Mass term

We consider time-reversal-symmetric perturbations that can open band gaps at the Dirac cones of Eq. (1). While the S_z-mixing SOC, which is naturally present in real materials, offers an illustrative example of such perturbations, here we introduce a general mass term. Consider the operation of time-reversal symmetry first:

$$\Theta\begin{pmatrix}R_1\\L_2\end{pmatrix}\Theta^{-1}=\begin{pmatrix}L_1\\-R_2\end{pmatrix}\text{ and }\Theta\begin{pmatrix}R_1^\dagger\\L_2^\dagger\end{pmatrix}\Theta^{-1}=\begin{pmatrix}L_1^\dagger\\-R_2^\dagger\end{pmatrix} \tag{5}$$

with the time-reversal symmetry operator Θ. This allows us to regard the Hamiltonian in Eq.(1) as a sum of two time-reversal related sub-Hamiltonians $H_0^{(+)}(x)$ and $H_0^{(-)}(x)=\Theta H_0^{(+)}(x)\Theta^{-1}$:

$$\begin{aligned}H_0(x)&=H_0^{(+)}(x)+H_0^{(-)}(x),\\H_0^{(+)}(x)&=-iv_1R_1^\dagger\partial_xR_1+iv_2L_2^\dagger\partial_xL_2\\H_0^{(-)}(x)&=iv_1L_1^\dagger\partial_xL_1-iv_2R_2^\dagger\partial_xR_2.\end{aligned} \tag{6}$$

The $H_0^{(\pm)}(x)$ here can be understood as describing the Dirac fermion around $\pm k_0$.

Hence, if the mass term in one of the sub-Hamiltonians, say, $H_M^{(+)}(x)$, is given by

$$me^{-i\theta}R_1^\dagger L_2+me^{i\theta}L_2^\dagger R_1, \tag{7}$$

with $m>0$, then the mass term in the full Hamiltonian can be obtained through:

$$\begin{aligned}H_M=&H_M^{(+)}(x)+H_M^{(-)}(x)\\=&H_M^{(+)}(x)+\Theta H_M^{(+)}(x)\Theta^{-1}\\=&(me^{-i\theta}R_1^\dagger L_2+\text{H.c.})+\left(me^{-i(\theta+\pi)}R_2^\dagger L_1+\text{H.c.}\right).\end{aligned} \tag{8}$$

There will thus be a π phase difference between the mass terms of the two sub-Hamiltonians $H_M^{(+)}(x)$ and $H_M^{(-)}(x)$, as indicated in Fig. 2.

Using Eq. (A1)–(A5), Eq. (8) can be rewritten as:

$$H_M^{(B)}=\frac{2m}{\pi a}\cos(\sqrt{2\pi}\vartheta_d)\sin(\theta+\sqrt{2\pi}\varphi_c), \tag{9}$$

which has minima at

$$\vartheta_d=\left(n+\frac{1}{2}\pm\frac{1}{2}\right)\sqrt{\frac{\pi}{2}},\ \varphi_c=-\frac{\theta}{\sqrt{2\pi}}+\left(n'\pm\frac{1}{2}\right)\sqrt{\frac{\pi}{2}}, \tag{10}$$

with $n,n'\in 2\mathbb{Z}$.

Notably, the mass terms here are generated by perturbations that do not close and reopen the bulk band gap and only influence the low-energy theory and hardly change the Fermi velocities determined by the overall band structure. Thus, the matrix elements of the H_M can be calculated by expanding the perturbation term ΔH in the Hamiltonian on the eigenstates of H_0, which we demonstrate in Sec. III through a concrete example.

B. Bulk-boundary correspondence

To derive the conserved current and hence the conserved charge in the system shown in Fig. 2, we use the following notation:

$$\begin{aligned}&\gamma^0=\begin{pmatrix}0&1\\1&0\end{pmatrix},\gamma^1=\begin{pmatrix}0&1\\-1&0\end{pmatrix},\gamma^5=\begin{pmatrix}-1&0\\0&1\end{pmatrix},\\&\psi_\mu=\begin{pmatrix}L_\mu\\R_\mu\end{pmatrix},\bar\psi_\mu=\psi_\mu^\dagger\gamma^0,\quad\mu=1,2.\end{aligned} \tag{11}$$

This allows us to rewrite the Hamiltonian with gap-opening perturbation $H=H_0+H_M$ as:

$$\begin{aligned}H=&-i\sum_\mu v\bar\psi_\mu\gamma^1\partial_x\psi_\mu+\delta v\epsilon^{\mu\nu}\bar\psi_\nu\gamma^1\partial_x\psi_\nu\\&+\sum_{\mu\neq\nu}\bar\psi_\mu(-m\cdot\cos\theta\gamma^5+(-1)^\mu i\cdot m\cdot\sin\theta\mathbb{I})\psi_\nu,\end{aligned} \tag{12}$$

with the corresponding Lagrangian:

$$\begin{aligned}L=&i\sum_\mu[v\bar\psi_\mu\partial\!\!\!/\psi_\mu-\delta v\epsilon^{\mu\nu}\bar\psi_\nu\partial\!\!\!/\psi_\nu]\\&-\sum_{\mu\neq\nu}\bar\psi_\mu[-m\cdot\cos\theta\gamma^5+(-1)^\mu i\cdot m\cdot\sin\theta\mathbb{I}]\psi_\nu.\end{aligned} \tag{13}$$

Thus, the conserved currents are

$$\begin{aligned}j^\sigma\propto&\sum_\mu\bar\psi_\mu\gamma^\sigma\psi_\mu-\frac{\delta v}{v}\epsilon^{\mu\nu}\bar\psi_\nu\gamma^\sigma\psi_\nu\\=&\sqrt{\frac{2}{\pi}}\left(\epsilon^{\sigma\eta}\partial_\eta\varphi_c+\frac{\delta v}{v}\epsilon^{\sigma\xi}\partial_\xi\varphi_d\right).\end{aligned} \tag{14}$$

and the total charge carried by the solitons is

$$Q_s^0\propto e\int j^0dx=e\sqrt{\frac{2}{\pi}}\int\left(\partial_x\varphi_c-\frac{\delta v}{v}\partial_x\varphi_d\right)dx, \tag{15}$$

where e is the electron charge. Through Eq. (10), we approximate $\partial_\mu\varphi_c\cong\frac{-1}{\sqrt{2\pi}}\partial_\mu\theta$ near the minimum of $H_M^{(B)}$ and apply Eqs. (A4)–(A5) to Eq. (15):

$$\begin{aligned}Q_s^0\cong&-\frac{e}{\pi}\int\left[\partial_x\theta+\pi\frac{\delta v}{v}(n_1-n_2)\right]dx\\=&-\frac{e}{2\pi}2[\theta(x\to\infty)-\theta(x\to-\infty)]-e\frac{\delta v}{v}(N_1-N_2),\end{aligned} \tag{16}$$

where n_i and N_i are the particle-number density and the particle number of the ith time-reversal sector, respectively. Since we are considering edge states of a 2D system, it is reasonable to assume identical chemical potentials for the two time-reversal sectors, given that these sectors are located at the system edges and analyzed in the absence of external fields that might tilt the Fermi level. Notably, this scenario only covers gap-opening perturbations that do not significantly alter the chemical potential, leaving the particle numbers unaffected. As a result, we have the same particle number $N_1=N_2$ and therefore,

$$Q_s^0=-\frac{e}{2\pi}2[\theta(x\to\infty)-\theta(x\to-\infty)]. \tag{17}$$

Note that, since e is negative, the soliton charge Q_s^0 is positive, and the soliton particle number $N_s = \frac{Q_s^0}{e}$ is negative. While we focus on time-reversal-invariant systems here, Eq. (17) can apply to systems without time-reversal symmetry, indicating that the soliton pairs can be created by applying time-reversal-symmetry-breaking perturbations that gap the edge states protected by some symmetries [23,24], see Appendix C).

Since the charge density j^0 is proportional to $\partial_x\theta$ according to the above approximations, a soliton appears around a spatial point where θ develops a kink. For smooth and clean edges where local perturbations due to spatial inhomogeneity are absent, we expect such a kink in θ only around a corner at which the adjacent edges are characterized by different values of θ. Therefore, the bulk-boundary correspondence implies that the total soliton charge Q_s^0 around a corner (i.e., the boundary of a 1D system) can be obtained from the phase difference between the mass terms $\theta(x \to \pm\infty)$ on the adjacent edges (i.e., the bulk of a 1D system). From the perspective of the two time-reversal sectors described by Eq. (6), the total soliton charge can be considered as the contribution of two identical soliton charges. Each sub-Hamiltonian features exponentially localized domain-wall states at the edge intersections (i.e., the corner). Hence, we can expect pairs of identical soliton excitations localized around the corner and generate in-gap corner modes with extra charges. This intuitive view can be readily understood by changing the basis:

$$\begin{pmatrix} \varphi_- \\ \varphi_+ \\ \vartheta_- \\ \vartheta_+ \end{pmatrix} = \frac{1}{2}\begin{pmatrix} 1 & 1 & 1 & -1 \\ 1 & 1 & -1 & 1 \\ 1 & -1 & 1 & 1 \\ -1 & 1 & 1 & 1 \end{pmatrix}\begin{pmatrix} \varphi_1 \\ \varphi_2 \\ \vartheta_1 \\ \vartheta_2 \end{pmatrix}. \tag{18}$$

In the new basis $(\varphi_+ \quad \varphi_- \quad \vartheta_+ \quad \vartheta_-)^T$, the bosonized Hamiltonian becomes:

$$H^{(B)} = H_+^{(B)} + H_-^{(B)},$$

where $H_\pm^{(B)}$ are

$$H_\pm^{(B)} = \frac{v}{2}\left[(\partial_x\varphi_\pm)^2 + (\partial_x\vartheta_\pm)^2 \mp \frac{2\delta v}{v}\partial_x\varphi_\pm\partial_x\vartheta_\pm\right] + \frac{m}{\pi a}\cos\left(\sqrt{4\pi}\varphi_\pm + \theta - \frac{\pi}{2}\right). \tag{19}$$

According to Eqs. (A3) and (A5), $H_\pm^{(B)}$ can be regarded as the bosonized sub-Hamiltonian describing the massive Dirac fermions at the momenta $\pm k_0$ in Fig. 2. For a typical case, we have $\frac{\delta v}{v} \ll 1$ such that terms with $\frac{\delta v}{v}$ can be neglected, and $H_\pm$ can be regarded as Gaussian models with the sine-Gordon terms [31–33]. The coupling constants in Eq. (19) correspond to the kink solution instead of the breather solution in a sine-Gordon problem, indicating each of $H_\pm^{(B)}$ produces the same amount of topological charge [32,33].

As further discussed below, instead of having topological in-gap corner zero modes, we will have topologically protected extra charge around the corner. Note that this charge is calculated with respect to the ground state [2–4], which can be obtained through computing the charge fluctuation in a finite-sized thin film and summing the value around the corner:

$$\Delta\rho(x,y) = e\sum_{i=1}^{N_{\text{occ.}}}\langle\psi_i(x,y)|\psi_i(x,y)\rangle - eN_{\text{occ.}}^{(\text{site})}, \tag{20}$$

where $N_{\text{occ.}}$ is the number of occupied bands and $N_{\text{occ.}}^{(\text{site})}$ is the number of occupied bands per site. For convenience, we will employ particle number fluctuation $\Delta N(x,y) = \frac{\Delta\rho(x,y)}{e}$ in subsequent calculations.

C. Symmetry properties

Our focus in this paper is on time-reversal invariant systems, but the particle-hole and chiral symmetries can be broken by either the nonzero velocity difference $\delta v \neq 0$ or the coexistence of the two mass terms. In either case, the energy of the corner modes is not fixed at zero since the system is in class AII in one dimension, characterized by trivial topology [34]. We can, however, have topologically protected corner zero modes when the particle-hole and chiral symmetries are restored if we have $\delta v = 0$ with at most a single mass term, i.e., $\theta = \frac{n\pi}{2}, n \in \mathbb{Z}$ on all edges. In the latter case, the topological invariant will be characterized by $\mathbb{Z}_2$ of class DIII in one dimension [20,35]. For general cases with both broken time-reversal and particle-hole symmetries, the systems fall into class AIII characterized by $\mathbb{Z}$ in the presence of the chiral symmetry or class A without topological modes. Based on the these consideration, our system contains only topologically protected charges instead of states with fixed energies.

D. Fractionalization properties

Our theory implies an unusual relation between the charge and spin degree of freedom originating from the helical nature of the edge states of a spin Chern insulator. This is distinct from the related features discussed in the existing literature where the Fermi velocities of different energy bands lead to charge-spin mixing [36–40]. The charge degree of freedom is intertwined with the spin degree of freedom, see Appendix A, due to the helical edge states, so that they do not form independent sectors. Instead, it is the charge-difference sector that remains independent from the charge sector [18], and the two sectors together describe the low-energy edge theory. Furthermore, the charge-difference sector denotes the deviation between the time-reversal subsystems; this is evident from Eq. (4), where it interacts with the charge sector due to a nonzero difference in Fermi velocity. Still, solitons, in our case, demonstrate an unusual spin-charge relationship. They feature spin-charge separated excitations, meaning that they carry fractional charges without spin [6], as depicted in Fig. 3(a). Due to time-reversal symmetry, there are no pure spinon excitations upon introducing many-body interactions. Instead, the many-body system hosts soliton and antisoliton excitations, carrying a fractional charge of $e \pm Q_s^0$. The two are related to each other by the time-reversal operator for half-integer spins [2,5,6,41], as indicated in Fig. 3(b).

E. Effect of interactions

Since the interaction between electrons is expected to play a role in the 1D edges [33], here we discuss its influence on the mass term through an RG analysis. To incorporate the interaction in Eq. (1), we include the forward scattering in

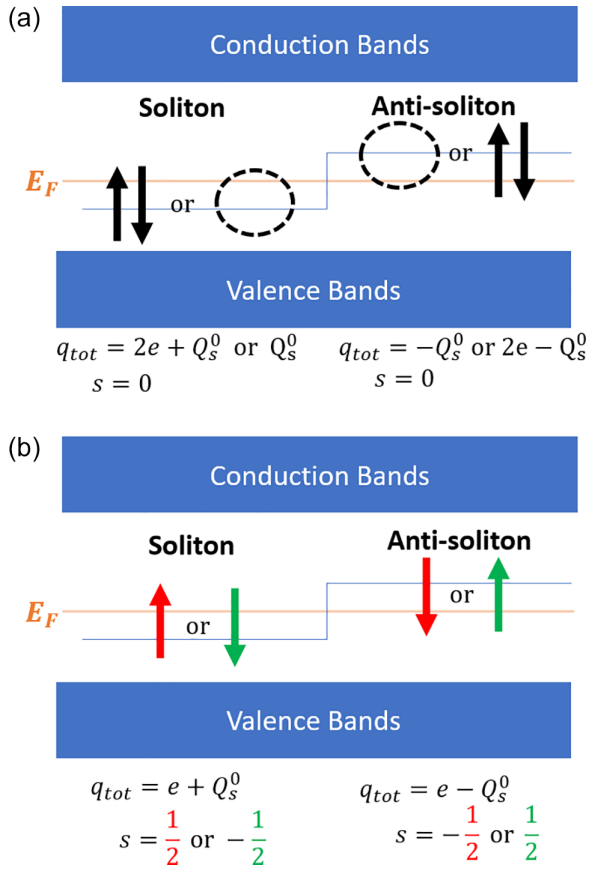

FIG. 3. (a) Due to time-reversal symmetry, a filled (anti)soliton excitation carries a net charge of $2e \pm Q_s^0$ without an associated spin while an empty (anti)soliton excitation carries a net charge of $\pm Q_s^0$ without an associated spin. The blue line indicates the energy level of the excitations while the orange line indicates the Fermi level. (b) In a time-reversal symmetric many-body system composed of soliton and antisoliton excitations, it is possible to have excitations with a half-integer spin and nonvanishing fractional charges $e \pm Q_s^0$ for (anti)solitons. The colors of the arrows indicate different time-reversal pairs.

each time-reversal sector after bosonization [19] and obtain two copies of a helical Luttinger liquid with the corresponding interaction parameters K_1, K_2 characterizing the interaction strength in each sector:

$$H_0^{(B)} = \frac{1}{2}\sum_{\mu=1}^{2} v_\mu \left[K_\mu^{-1}(\partial_x \varphi_\mu)^2 + K_\mu(\partial_x \vartheta_\mu)^2\right]. \tag{21}$$

In the basis $(\varphi_1 \quad \varphi_2 \quad \vartheta_1 \quad \vartheta_2)^T$, Eq. (9) can be rewritten as:

$$H_M^{(B)} = \frac{2m}{\pi a}\cos[\sqrt{\pi}(\vartheta_1 - \vartheta_2)]\sin[\theta + \sqrt{\pi}(\varphi_1 + \varphi_2)]. \tag{22}$$

If we define $\tilde{m} \equiv \frac{m}{\sqrt{v_1 v_2}} a$, the RG flow equations can be obtained from the standard procedure [19,33,42]:

$$\frac{dK_\mu}{dl} = -\tilde{m}^2 \frac{K_\mu^2 - 1}{2}, \tag{23}$$

$$\frac{d\tilde{m}}{dl} = \left[2 - \frac{1}{4}\sum_\mu \left(K_\mu + K_\mu^{-1}\right)\right]\tilde{m}, \tag{24}$$

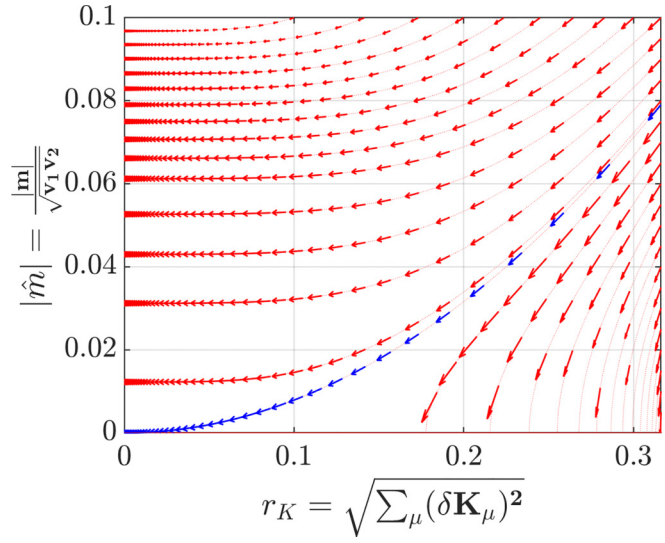

FIG. 4. Solution of the RG flows in Eqs. (26) and (27) described by Eqs. (28) and (29). The blue trajectory indicates the critical points where $r_K(l=0) = 4\hat{m}(l=0)$.

where we have set $a = a_0 e^l$ with the short-distance cutoff a_0. Note that Eq. (24) can be written as:

$$\frac{dm}{dl} = \left[1 - \frac{1}{4}\sum_\mu \left(K_\mu + K_\mu^{-1}\right)\right]m. \tag{25}$$

Since $K_\mu + K_\mu^{-1} \geqslant 2$, the corresponding operator in Eq. (22) is at most marginally relevant in the RG sense. It can be seen from Eqs. (23) and (24) that K_μ and m tend to flow toward the fixed points $(K_\mu, m) \to (1, m^*)$ or $(K_\mu^*, 0)$, with some renormalized values m^* and K_μ^*. Intuitively, when $K_\mu(l=0)$ deviates from unity, m decreases to zero faster than the evolution of K_μ to unity. Otherwise, the sine-Gordon term is marginal, and the system scales as its noninteracting version. To demonstrate this behavior, we analyze the RG flow around the fixed point $K_\mu = 1$ by setting $K_\mu = 1 + \delta K_\mu$ with $\delta K_\mu \ll 1$ and expanding Eqs. (23) and (24) to the third-order of perturbations p, where $p \in \{\delta K_\mu, m\}$. This procedure gives:

$$\frac{d(\delta K_\mu)^2}{dl} = -2\tilde{m}^2(\delta K_\mu)^2, \tag{26}$$

$$\frac{d\tilde{m}^2}{dl} = \left[2 - \frac{1}{4}\sum_\mu (\delta K_\mu)^2\right]\tilde{m}^2. \tag{27}$$

By setting $x_\pm = \tilde{m}^2 \pm \frac{1}{8}\sum_\mu (\delta K_\mu)^2$, we can solve Eqs. (26) and (27) exactly. The solutions after transforming $x_\pm$ back into $\hat{m} \equiv \frac{\tilde{m}}{a} = \frac{m}{\sqrt{v_1 v_2}}$, $r_K = \sqrt{\sum_\mu (\delta K_\mu)^2}$ are

$$r_K(l) = r_K(l=0)e^{-l}, \tag{28}$$

$$\hat{m}^2(l) = \hat{m}^2(l=0) + \frac{e^{-4l} - 1}{16} r_K^2(l=0). \tag{29}$$

The trajectories of Eqs. (28) and (29) with several sets of initial values $\{r_K(l=0)\}$ and $\{\hat{m}(l=0)\}$ are plotted in Fig. 4. According to Eqs. (28) and (29), m becomes irrelevant when $r_K(l=0) \geqslant 4\hat{m}(l=0)$. On the other hand, the sine-Gordon

term characterized by m is marginal at large l when $r_K(l = 0) < 4\hat{m}(l = 0)$, which can be better captured if we expand Eqs. (23) and (25) only to the first order of δK_μ:

$$\frac{d\delta K_\mu}{dl} = -\tilde{m}^2 \delta K_\mu, \tag{30}$$

$$\frac{dm}{dl} = 0. \tag{31}$$

Equations (30) and (31) indicate that $|\delta K_\mu|$ decreases due to finite m while m remains unchanged during the RG flow.

We make two remarks regarding the RG analysis: (i) Eq. (1) does not contain intersector forward scattering terms. Incorporating these terms would result in additional terms, such as $\partial_x\varphi_1\partial_x\varphi_2$, entering Eq. (21) in the bosonized form. While symmetry considerations generally allow these terms, they do not lead to gap opening, i.e., they do not contribute directly to the emergence of new mass terms. Moreover, similar analysis on two-sub-band quantum wires showed that systems with finite inter-sub-band forward scattering would evolve towards a fixed point characterized by two independent channels [43]. In the RG framework, these marginal terms could, in principle, modify the renormalized values of the mass, as demonstrated in Appendix D. (ii) While Fig. 4 describes the RG flow in an infinite system, the RG flow in realistic systems can be stopped earlier due to finite size or finite temperature, thus preventing it from reaching the gapless fixed point with $m = 0$ [19,44]. For instance, in a finite edge, the RG flow only evolves up to the scale $l \sim \ln(L/a_0)$ with the edge length L, where the system has finite mass terms characterized by the renormalized m^* value. As a result, time-reversal soliton pairs can still exist in a finite-sized thin film, even in an interacting system where K_μ deviates from unity.

III. APPLICATION TO AN EXTENDED HALDANE MODEL

We turn now to illustrate the previous results with the example of a time-reversal-symmetric extension of the Haldane model [24]. Before adding the S_z-mixing SOC, gapless edge states emerge due to its spin Chern number $C_s = 2$. The presence of S_z-mixing SOC opens small gaps in the edge band structure. The Hamiltonian of this model is

$$\begin{aligned} H = &\sum_\sigma [d_1(\vec{k}) a_\sigma^\dagger b_\sigma - i d_2(\vec{k}) a_\sigma^\dagger b_\sigma + \text{H.c.} \\ &+ (d_3(\vec{k})\text{sign}(\sigma) + m)(a_\sigma^\dagger a_\sigma - b_\sigma^\dagger b_\sigma)] \\ &+ i\lambda_R \sum_{j=1}^{3} (\vec{c}_j \times \vec{S})_z^{\sigma\sigma'} e^{i\vec{k}\cdot\vec{c}_j} a_\sigma^\dagger b_{\sigma'} + \text{H.c.}, \end{aligned} \tag{32}$$

where σ is the spin index where $a_\sigma^\dagger, b_\sigma^\dagger$ is the creation operator for spin σ electron on a different sublattice. The $d_1(\vec{k}), d_2(\vec{k}), d_3(\vec{k})$ are defined as: $d_1 = \sum_{j=1}^{3}[t_1 \cos(\vec{k}\cdot\vec{a}_j) + t_3 \cos(\vec{k}\cdot\vec{c}_j)]$, $d_2 = \sum_{j=1}^{3}[-t_1 \sin(\vec{k}\cdot\vec{a}_j) - t_3 \sin(\vec{k}\cdot\vec{c}_j)]$, and $d_3 = \sum_{j=1}^{6} t_2(-1)^j \sin(\vec{k}\cdot\vec{b}_j)$, where $\vec{a}_j, \vec{b}_j, \vec{c}_j$ are the vectors connecting a site to its first-, second-, and third-nearest neighbors on a honeycomb lattice, respectively. Notably, both the second-nearest-neighbor hopping t_2 and the third-nearest-neighbor hopping t_3 are crucial for having a high spin Chern number, although their strength should be sufficiently large

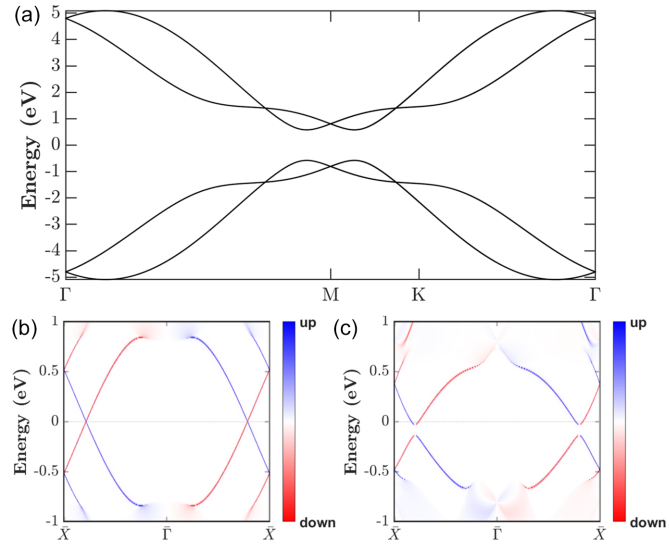

FIG. 5. (a) Bulk band structure of the Hamiltonian in Eq. (32). (b) Spin-resolved spectrum of the gapless edge states. (c) Spin-resolved spectrum of the edge states that are gapped by the Rashba SOC. The Dirac cones shift toward the Brillouin zone boundary in k space and to lower energy due to the Rashba SOC.

($t_2 > 0.3t_1$ and $t_3 > 0.4t_1$) for the model to have a spin Chern number greater than unity [24].

In the following calculations, we set $t_1 = 1$, $m = 0.1$, $\lambda_R = 0.3$, and $t_2 = t_3 = 0.6$. With these parameters, the model has spin Chern number $C_s = 2$ and S_z-mixing SOC gaps of edge states on its armchair edges (Fig. 5). In both cases, the centers of the gapped Dirac cones are shifted in both k-space and energy, indicating the presence of a k-dependent mass term in the low-energy theory. As a zeroth-order approximation in k for the mass term, our theory still properly captures features of low-energy theories.

After the Rashba SOC gaps the edge states, the in-gap corner modes emerge in a finite-sized armchair-edged thin film [Fig. 6(a)], and the extra charges accumulate around the corner of the thin film [Fig. 6(b)].

Edge Hamiltonian for an arbitrary edge

Here, we derive the effective edge Hamiltonian for an arbitrary edge to demonstrate how Rashba SOC induces the edge mass kink in the model described by Eq. (32). The Bloch

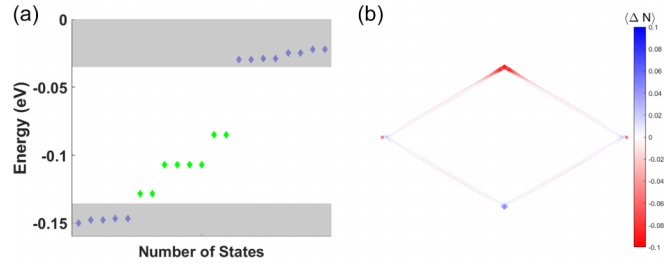

FIG. 6. (a) Spectrum of a 60a×60a thin film, in which the in-gap corner modes are marked in green. (b) Particle-number fluctuation ΔN with respect to the ground state in a 60a×60a thin film. Here, a is the lattice constant.

Hamiltonian of Eq. (32) is

$$\begin{aligned}H=&\left\{t_1\left[1+\cos\left(\frac{k_x+\sqrt{3}k_y}{2}\right)+\cos\left(\frac{-k_x+\sqrt{3}k_y}{2}\right)\right]\right\}\sigma_0\tau_1\\&+\left\{t_1\left[1+\sin\left(\frac{k_x+\sqrt{3}k_y}{2}\right)+\sin\left(\frac{-k_x+\sqrt{3}k_y}{2}\right)\right]\right\}\sigma_0\tau_2\\&+\{t_3[2\cos(k_x)+\cos(\sqrt{3}k_y)]\}\sigma_0\tau_1+[t_3\sin(\sqrt{3}k_y)]\sigma_0\tau_2\\&+2t_2\left[\sin\left(\frac{k_x+\sqrt{3}k_y}{2}\right)-\sin\left(\frac{-k_x+\sqrt{3}k_y}{2}\right)\right]\sigma_3\tau_3\\&+m\sigma_0\tau_3-2t_2\sin(k_x)\sigma_3\tau_3\\&+2\lambda_R\sin(\sqrt{3}k_y)\sigma_1\tau_1-2\sqrt{3}\lambda_R\sin(k_x)\sigma_2\tau_1\\&+4\lambda_R\sin\left(\frac{k_x+\sqrt{3}k_y}{2}\right)\sin\left(\frac{-k_x+\sqrt{3}k_y}{2}\right)\sigma_1\tau_2,\end{aligned}\tag{33}$$

where σ (τ) are the Pauli matrices in the spin (sublattice) degree of freedom. According to its band structure (Fig. 5), the low-energy Hamiltonian is obtained by expanding (k_x, k_y) around the point M in the Brillouin zone:

$$\begin{aligned}H=&(3t_3-t_1)\sigma_0\tau_1+[t_1+\sqrt{3}(t_3-t_1)k_y]\sigma_0\tau_2+m\sigma_0\tau_3\\&+2\sqrt{3}\lambda_R(k_y\sigma_1\tau_1-k_x\sigma_2\tau_1).\end{aligned}\tag{34}$$

To understand the low-energy Hamiltonian on arbitrary edges, we describe the coordinates in the low-energy Hamiltonian with a new basis set [11,13]:

$$\begin{pmatrix}k_x\\k_y\end{pmatrix}=\begin{pmatrix}\sin(\xi)&\cos(\xi)\\-\cos(\xi)&\sin(\xi)\end{pmatrix}\begin{pmatrix}k_1\\k_2\end{pmatrix},\tag{35}$$

and obtain the edge Hamiltonian by replacing k_1 with $-i\partial_x$ and k_2 with $\pm k_0$, where k_0 is the k point of the Dirac cones in the edge Brillouin zone:

$$\begin{aligned}H=&(3t_3-t_1)\sigma_0\tau_1+m\sigma_0\tau_3\\&+[t_1+\sqrt{3}(t_3-t_1)(i\cos(\xi)\partial_x\pm k_0\sin(\xi)]\sigma_0\tau_2\\&+2\sqrt{3}\lambda_R[i\cos(\xi)\partial_x\pm k_0\sin(\xi)]\sigma_1\tau_1\\&-2\sqrt{3}\lambda_R[-i\sin(\xi)\partial_x\pm k_0\cos(\xi)]\sigma_2\tau_1.\end{aligned}\tag{36}$$

By using the ansatz $e^{\eta x}\phi$, we can obtain the chiral edge states before adding the Rashba term:

$$\begin{aligned}|R_\pm\rangle&=N_\pm\left(\tfrac{A_\pm(\xi)e^{i\phi_\pm(\xi)}}{m}\quad -1\quad 0\quad 0\right)^T,\\|L_\pm\rangle&=N_\pm\left(0\quad 0\quad \tfrac{A_\pm(\xi)e^{i\phi_\pm(\xi)}}{m}\quad -1\right)^T,\end{aligned}\tag{37}$$

and the Rashba term:

$$\begin{aligned}&i2\sqrt{3}\lambda_R\{[\eta\cos(\xi)\mp ik_0\sin(\xi)]\sigma_1\\&\quad+[\eta\sin(\xi)+ik_0\cos(\xi)]\sigma_2\}\tau_1,\end{aligned}\tag{38}$$

where:

$$\begin{aligned}A_\pm(\xi)&=\|(3t_3-t_1)-i[t_1+\sqrt{3}(t_3-t_1)k_\pm]\|,\\\phi_\pm(\xi)&=\mathrm{Arg}[(3t_3-t_1)-i(t_1+\sqrt{3}(t_3-t_1)k_\pm)]\\k_\pm&=i\eta\cos(\xi)\pm k_0\sin(\xi),\end{aligned}$$

and $N_\pm$ is the normalization factor. Since the edge states are very localized, we assume $\eta\gg 1$ such that Eq. (38) can be approximated by:

$$i2\sqrt{3}\lambda_R\eta[\cos(\xi)\sigma_1+\sin(\xi)\sigma_2]\tau_1,\tag{39}$$

with $\phi_\pm(\xi)\cong 0$. The matrix elements $m_\pm$ of the mass term, for example, are $\langle R_\pm|\,\Delta H\,|L_\mp\rangle$, where ΔH is the Hamiltonian in Eq. (38). Therefore, the element $m_\pm$ is proportional to $e^{-i(\xi+\frac{\pi}{2})}$, which has different values on different edges, indicating that the Rashba SOC induces mass kinks on the edges. More specifically, the phase θ of the mass in Eq. (7) is given by $\theta=\xi+\frac{\pi}{2}$. Given that different edges correspond to distinct angles of edge orientation ξ, finite charges emerge at the corner located between any two adjacent edges. Denoting two such edges as edge 1 and edge 2, with their corresponding orientations ξ_1 and ξ_2, the value of the corner charge can be computed using Eq. (17) with $\theta(x\to\infty)=\xi_1$ and $\theta(x\to-\infty)=\xi_2$. This results in a nonzero value for the corner charge being proportional to $(\xi_1-\xi_2)$ between any pair of adjacent edges, given that the different edges are characterized by $\xi_1\neq\xi_2$. Note that such a charge, typically nonintegral, arises with any infinitesimal change in the angle between the edges, indicating that there is no critical angle required for the charge to appear.

Before concluding this section, we note that, while we have considered the extended Haldane model [Eq. (33)] as an example, the analysis outlined from Eq. (34) to Eq. (39) can be applied to material-specific tight-binding models with and without the spin-$U(1)$-symmetry-breaking SOC by expanding to linear order in k around the valley of the Dirac cones. With the coordinate transformation and substitution of momentum in Eq. (35), one can then obtain the effective edge Hamiltonian and the wave function of the corresponding helical edge states along the lines of Eqs. (36)–(38). The phase of the mass term can be determined by calculating the matrix element of the spin-$U(1)$-symmetry-breaking SOC as in Eq. (39) for the extended Haldane model.

IV. SUMMARY AND CONCLUSIONS

We derive the mass-kink mechanism in a 1D system with two bulk Dirac cones related by time-reversal symmetry using bosonization techniques. Bulk Dirac cones are shown to generate two solitons on the domain wall by imposing gap-opening time-reversal-symmetric perturbations. The value of the extra charge on the domain wall is thus twice the value of the phase difference in the mass term on the Dirac cones. The formalism is applied to the edge of a spin Chern insulator with $C_s=2$, in which the corner modes in a finite-sized thin film result from solitons generated through the mass-kink mechanism induced by S_z-mixing SOC. We consider the model proposed in Ref. [24] as an example. By investigating the phase evolution of the corner modes along the edge of a finite-sized thin film, we show that S_z-mixing SOC opens gapless

edge states and, as expected, induces solitons through the mass-kink mechanism. The phase evolutions also support the viewpoint that the pairwise in-gap corner modes are generated by distinct edge Dirac cones.

We also consider an HO topological phase with protected corner charges from a spin Chern insulator with $C_s = 2$. Since the complex mass term with the edge-dependent phase is generically present here (induced, for example, by the anisotropic S_z-mixing SOC), our analysis provides strong evidence that the results hold for general anisotropic systems with spin Chern number $C_s = 2$. Our formalism can be extended straightforwardly to treat systems with a larger number of time-reversal-related Dirac cones, indicating that time-reversal soliton pairs with protected corner charges can appear on the edges of spin Chern insulators with even spin Chern numbers $C_s = 2n(n > 1)$ more generally. Similar arguments would also apply to $\hat{w}$-Chern insulators with a nonzero even $\hat{w}$-Chern number and anisotropic $\hat{w}$-symmetry breaking perturbations [26,27,45]. For example, in a mirror-Chern insulator with an even mirror-Chern number [46], there are two gapless helical states protected by the out-of-plane mirror symmetry. When the mirror symmetry is broken by, for example, an in-plane Zeeman field, soliton pairs can arise with the same mechanism as the one mentioned in Ref. [47].

ACKNOWLEDGMENTS

The authors thank Yun-Chung Chen and Benjamin J. Wieder for useful discussions. The work at Northeastern University was supported by the National Science Foundation through NSF-ExpandQISE Award No. 2329067 and it benefited from Northeastern University's Advanced Scientific Computation Center and the Discovery Cluster. H.L. acknowledges the support by Academia Sinica in Taiwan under Grant No. AS-iMATE-113-15. C.-H.H. acknowledges the financial support from the National Science and Technology Council (NSTC), Taiwan through NSTC-112-2112-M-001-025-MY3.

APPENDIX A: BOSONIZATION CONVENTIONS

In this Appendix we present our bosonization conventions. By using the notation in Appendix A of Ref. [29], the Bosonic representations of the right- and left-moving modes are

$$R_\sigma(x) = \frac{\kappa_\uparrow}{\sqrt{2\pi a}} e^{i\sqrt{4\pi}\phi^R_\sigma(x)},$$
$$L_\sigma(x) = \frac{\kappa_\downarrow}{\sqrt{2\pi a}} e^{-i\sqrt{4\pi}\phi^L_\sigma(x)}, \tag{A1}$$

where $a \to 0$ is the bosonic UV cutoff, $\sigma = 1, 2$ denotes the time-reversal sector and κ_σ is the Klein factors satisfying $\{\kappa_\sigma, \kappa_{\sigma'}\} = 2\delta_{\sigma\sigma'}$ and $\kappa_\sigma^2 = 1, \kappa_\uparrow\kappa_\downarrow = -\kappa_\downarrow\kappa_\uparrow = i$. Since all right moving modes carry spin $\uparrow$ while all left moving modes carry spin $\downarrow$, we suppress the index for spin in Eq. (A1).

To have correct anticommutation relation $\{R_\sigma, L_\sigma\} = 0$ and $\{R_\sigma(x), R_\sigma(y)\} = 0$, the Boson field should follow the commutation relation:

$$\left[\phi^R_\sigma(x), \phi^L_{\sigma'}(x)\right] = \frac{i}{4}\delta_{\sigma\sigma'},$$
$$\left[\phi^\eta_\sigma(x), \phi^{\eta'}_{\sigma'}(y)\right] = \frac{i}{4}\eta\delta_{\eta\eta'}\delta_{\sigma\sigma'}\mathrm{sign}(x-y). \tag{A2}$$

The conjugated variables are defined as:

$$\varphi_\sigma \equiv \phi^R_\sigma + \phi^L_\sigma,$$
$$\vartheta_\sigma \equiv \phi^L_\sigma - \phi^R_\sigma. \tag{A3}$$

Then, we have:

$$R^\dagger_\sigma R_\sigma + L^\dagger_\sigma L_\sigma = \frac{1}{\sqrt{\pi}}\partial_x\varphi_\sigma. \tag{A4}$$

Further, we can define the charge degree of freedom and the charge-difference degree of freedom:

$$\varphi_c \equiv \frac{1}{\sqrt{2}}(\varphi_1 + \varphi_2),$$
$$\vartheta_c \equiv \frac{1}{\sqrt{2}}(\vartheta_1 + \vartheta_2),$$
$$\varphi_d \equiv \frac{1}{\sqrt{2}}(\varphi_1 - \varphi_2),$$
$$\vartheta_d \equiv \frac{1}{\sqrt{2}}(\vartheta_1 - \vartheta_2). \tag{A5}$$

Note that, by using Eqs. (A3) and (A4), we can get $\partial_x\vartheta_c \propto \rho_s$, where ρ_s is the spin density. The spin and charge degrees of freedom are related through these conjugated variables. Similarly, the spin and charge density differences are also related in the same way.

APPENDIX B: BASIC PROPERTIES OF BOSONIC FIELDS

Theorem 1. $[\varphi_\sigma(x), \partial_y\vartheta_\sigma(y)] = i\pi\delta(x-y), \sigma = 1, 2$

Proof. In our model, the fermionic annihilation operator ψ can be written as:

$$\psi = \sum_\sigma \left(\sum_{k>0} \frac{e^{ikx}}{\sqrt{L}} c_{k,\sigma} + \sum_{k<0} \frac{e^{ikx}}{\sqrt{L}} c_{k,\sigma} \right)$$
$$= \sum_\sigma \left(\sum_{k=-k_0}^{\infty} \frac{e^{i(k+k_0)x}}{\sqrt{L}} C_{k+k_0,\sigma} + \sum_{k=-\infty}^{k_0} \frac{e^{i(k-k_0)x}}{\sqrt{L}} c_{k-k_0,\sigma} \right)$$
$$\equiv e^{ik_0x}(R_1 + L_2) + e^{-ik_0x}(R_2 + L_1), \tag{B1}$$

where $L \to \infty$ is the size of the system and $\psi(x+L) = \psi(x)$ is satisfied. The right- (left)-moving modes are defined as:

$$R_1 = \sum_k \frac{e^{ikx}}{\sqrt{L}} C^{R_1}_k, C^{R_1}_k \equiv C_{k+k_0,\uparrow}$$

$$L_1 = \sum_k \frac{e^{-ikx}}{\sqrt{L}} C^{L_1}_k, C^{L_1}_k \equiv C_{-(k+k_0),\downarrow}$$

$$R_2 = \sum_k \frac{e^{ikx}}{\sqrt{L}} C_k^{R_2},\ C_k^{R_2} \equiv C_{k-k_0,\uparrow}$$
$$L_2 = \sum_k \frac{e^{-ikx}}{\sqrt{L}} C_k^{L_2},\ C_k^{L_2} \equiv C_{-k+k_0,\downarrow} \tag{B2}$$

In this definition, the right- (left)-moving modes are filled when $k < 0$ in each summation.

Then, following [48], each right- (left)-moving mode is the coherent state of the corresponding Boson field:

$$\begin{aligned}\left[b_q^{R_\mu}, R_\mu\right] &= \sqrt{\frac{2\pi}{L^2|q|}}\left[\sum_k c_{k-q}^{(R_\mu)\dagger} c_k^{R_\mu}, \sum_{k'} e^{ik'x} c_{k'}^{R_\mu}\right] \\ &= -\sqrt{\frac{2\pi}{|q|}}\frac{1}{L}\sum_{k,k'} \delta_{k-q,k'} e^{ik'x} c_k^{R_\mu} \\ &= -\sqrt{\frac{2\pi}{|q|L}} e^{-iqx} R_\mu, \end{aligned} \tag{B3}$$

$$\begin{aligned}\left[b_q^{L_\mu}, L_\mu\right] &= \sqrt{\frac{2\pi}{L^2|q|}}\left[\sum_k c_{k-q}^{(L_\mu)\dagger} c_k^{L_\mu}, \sum_{k'} e^{-ik'x} c_{k'}^{L_\mu}\right] \\ &= -\sqrt{\frac{2\pi}{|q|}}\frac{1}{L}\sum_{k,k'} \delta_{k-q,k'} e^{-ik'x} c_k^{L_\mu} \\ &= -\sqrt{\frac{2\pi}{|q|L}} e^{iqx} L_\mu, \end{aligned} \tag{B4}$$

where $b_q^{R_\mu(L_\mu)}$ is the Bosonic annihilation operator for the density fluctuation of each right- (left)-moving mode. Since R_μ, L_μ satisfy the commutation relation for the right- (left)-moving modes defined in Ref. [48] for each μ. Therefore, as derived for the right- (left)-moving modes in Ref. [48], $[\varphi_\mu(x), \partial_y \vartheta_\mu(y)] = i\pi\delta(x-y)$ for $\mu = 1, 2$ denoting the time-reversal sector.

Theorem 1 shows that φ_μ and ϑ_μ are indeed canonical conjugate variables. By using Theorem 1, the commutation relation $[\varphi_{c(d)}(x), \partial_y \vartheta_{c(d)}(y)] = i\pi\delta(x-y)$ can also be proven, which means that the boson field and its dual field in the charge sector and charge-difference sector are canonical conjugate variables, too. Besides, this also provides a foundation for Eq. (A4) by using the corresponding derivation in Ref. [48].

APPENDIX C: GENERAL MASS TERM

In general, the gap-opening perturbation need not be time-reversal symmetric. Therefore, the phases of the mass term of different Dirac cones can differ by an arbitrary phase α. Then, Eq. (8) becomes:

$$H_M = me^{-i\theta} R_1^\dagger L_2 + me^{-i(\theta+\alpha)} R_2^\dagger L_1 + \text{H.c.}, \tag{C1}$$

which can be further bosonized into:

$$\begin{aligned} H_M^{(B)} = \frac{m}{\pi a}\big(&\sin(\sqrt{2\pi}(\varphi_c - \vartheta_d) + \theta) \\ &+ \sin[\sqrt{2\pi}(\varphi_c + \vartheta_d) + \theta + \alpha + \pi)]. \end{aligned} \tag{C2}$$

It has minima at,

$$\vartheta_d = -\frac{\alpha+\pi}{2\sqrt{2\pi}} + (n'-n)\frac{\sqrt{\pi}}{2}, \tag{C3}$$
$$\varphi_c = -\frac{\theta}{\sqrt{2\pi}} - \frac{\alpha+\pi}{2\sqrt{2\pi}} + (n'+n-1)\frac{\sqrt{\pi}}{2}, \tag{C4}$$

for some $n', n \in \mathbb{Z}$. Therefore, the approximation made in Eq. (16) remains valid. That is, there are always extra charges around the corner as long as a k-independent perturbation opens the gapless surface Dirac cones that generate different phases of the mass term on adjacent edges. The amount of the extra charge can then be calculated through Eq. (17).

APPENDIX D: INFLUENCE OF INTERSECTOR FORWARD SCATTERING

In this Appendix, we discuss the effect of intersector forward scatterings on the RG flow. In the main text, we included the following intrasector forward scatterings in our bosonized model H_0 described by Eq. (21),

$$\begin{aligned} H_{\text{intra}} = \sum_{\mu=1,2} &\frac{g_{4,\mu}^{(\text{intra})}}{2}(R_\mu^\dagger R_\mu R_\mu^\dagger R_\mu + L_\mu^\dagger L_\mu L_\mu^\dagger L_\mu) \\ &+ \frac{g_{2,\mu}^{(\text{intra})}}{2}(R_\mu^\dagger R_\mu L_\mu^\dagger L_\mu + \text{H.c.}). \end{aligned} \tag{D1}$$

While intersector forward scattering terms are typically omitted, as is the case in bosonized models for multichannel systems [49,50], in general, the intersector forward scatterings can be considered,

$$\begin{aligned} H_{\text{inter}} =& \frac{g_4^{(\text{inter})}}{2}(R_1^\dagger R_1 R_2^\dagger R_2 + L_1^\dagger L_1 L_2^\dagger L_2 + \text{H.c.}) \\ &+ \frac{g_2^{(\text{inter})}}{2}(R_1^\dagger R_1 L_2^\dagger L_2 + R_2^\dagger R_2 L_1^\dagger L_1 + \text{H.c.}). \end{aligned} \tag{D2}$$

Since $H_0 + H_{\text{inter}}$ is still quadratic in terms of the bosonic fields, it can be diagonalized. For simplicity, in the following we approximate $v_1 \cong v_2 \equiv v$, applicable for most materials, as well as $g_{4,\mu=1}^{(\text{intra})} = g_{4,\mu=2}^{(\text{intra})} \equiv g_4^{(\text{intra})}$ and $g_{2,\mu=1}^{(\text{intra})} = g_{2,\mu=2}^{(\text{intra})} \equiv g_2^{(\text{intra})}$.

With the inclusion of intersector forward scatterings in Eq. (D2) and the above assumptions, the bosonized Hamiltonian can be diagonalized into:

$$H_0 + H_{\text{inter}} = \frac{1}{2}\sum_{\mu=c,d} u_\mu K_\mu^{-1}(\partial_x \varphi_\mu)^2 + u_\mu K_\mu (\partial_x \vartheta_\mu)^2, \tag{D3}$$

with the modified interaction parameters,

$$\begin{aligned} K_c &= \sqrt{\frac{v + \tilde{g}_4^{(\text{intra})} - \tilde{g}_2^{(\text{intra})} + \tilde{g}_4^{(\text{inter})} - \tilde{g}_2^{(\text{inter})}}{v + \tilde{g}_4^{(\text{intra})} + \tilde{g}_2^{(\text{intra})} + \tilde{g}_4^{(\text{inter})} + \tilde{g}_2^{(\text{inter})}}} \\ K_d &= \sqrt{\frac{v + \tilde{g}_4^{(\text{intra})} - \tilde{g}_2^{(\text{intra})} - \tilde{g}_4^{(\text{inter})} + \tilde{g}_2^{(\text{inter})}}{v + \tilde{g}_4^{(\text{intra})} + \tilde{g}_2^{(\text{intra})} - \tilde{g}_4^{(\text{inter})} - \tilde{g}_2^{(\text{inter})}}}, \end{aligned} \tag{D4}$$

and renormalized velocities:

$$\begin{aligned} u_c =& (v + \tilde{g}_4^{(\text{intra})} - \tilde{g}_2^{(\text{intra})} + \tilde{g}_4^{(\text{inter})} - \tilde{g}_2^{(\text{inter})})/K_c \\ u_d =& (v + \tilde{g}_4^{(\text{intra})} - \tilde{g}_2^{(\text{intra})} - \tilde{g}_4^{(\text{inter})} + \tilde{g}_2^{(\text{inter})})/K_d, \end{aligned} \tag{D5}$$

where $\tilde{g}_4^{(\text{intra})} = \frac{1}{4\pi} g_4^{(\text{intra})}$, $\tilde{g}_2^{(\text{intra})} = \frac{1}{4\pi} g_2^{(\text{intra})}$, $\tilde{g}_4^{(\text{inter})} = \frac{1}{4\pi} g_4^{(\text{inter})}$, $\tilde{g}_2^{(\text{inter})} = \frac{1}{4\pi} g_2^{(\text{inter})}$. On this basis, the mass term in Eq. (9) is used to proceed with the RG analysis.

The RG flow equations can be derived as:

$$\frac{d\tilde{m}}{dl} = \left[2 - \frac{1}{2}\left(K_c + K_d^{-1}\right)\right]\tilde{m} \tag{D6}$$

$$\frac{dK_c}{dl} = -K_c^2 \tilde{m}^2 \tag{D7}$$

$$\frac{dK_d}{dl} = \tilde{m}^2, \tag{D8}$$

with $\tilde{m} \equiv \frac{m \sin(\theta)}{\sqrt{u_c u_d}\pi} a$. The above equations demonstrate that the mass term is RG relevant for repulsive interactions, thereby stabilizing the predicted corner modes.

To obtain further insight into the effect of intersector forward scatterings, we consider a weak intersector forward scattering such that $\tilde{g}_{2(4)}^{(\text{inter})} \ll \tilde{g}_{2(4)}^{(\text{intra})}$. We can then approximate the Luttinger liquid parameters to the first order of $g_{2(4)}^{(\text{inter})}$:

$$\begin{aligned} K_c \cong& K + \delta K \\ K_d \cong& K - \delta K, \end{aligned} \tag{D9}$$

where $\delta K \ll K$. Here:

$$\begin{aligned} K \equiv& \sqrt{\frac{v + \tilde{g}_4^{(\text{intra})} - \tilde{g}_2^{(\text{intra})}}{v + \tilde{g}_4^{(\text{intra})} + \tilde{g}_2^{(\text{intra})}}} \\ \delta K \equiv& \frac{-g_2^{(\text{inter})}}{\sqrt{\left(v + \tilde{g}_4^{(\text{intra})}\right)^2 - \left(\tilde{g}_2^{(\text{intra})}\right)^2}}. \end{aligned} \tag{D10}$$

Then, the dominant contributions in the RG flow equations become:

$$\frac{dK}{dl} = -\frac{\tilde{m}^2}{2}(K^2 - 1) \tag{D11}$$

$$\frac{d\tilde{m}}{dl} = \left[2 - \frac{1}{2}\left(K + \frac{1}{K}\right)\right]\tilde{m}. \tag{D12}$$

$$\frac{d\delta K}{dl} = -\frac{\tilde{m}^2}{2}(K^2 + 1). \tag{D13}$$

Note that the interaction parameter K in Eq. (D10) is the Luttinger liquid parameter in the absence of the intersector forward scatterings. Hence, Eqs. (D11)–(D12) recover Eqs. (23)–(24) by identifying $K_1 = K_2 = K$ in Eqs. (23) and (24). On the other hand, the change in the interaction strength arising from the intersector forward scattering is represented by δK. While $|\delta K|$ exhibits a monotonic increase along the RG process according to Eqs. (D10) and (D13), leading to contributions to the renormalized K_c and K_d values, we note that the RG flow will eventually stop due to the finite system size or temperature, as discussed in the main text. Moreover, according to Eq. (D12), the flow of $\tilde{m}$ is not affected by δK as long as $\delta K \ll K$. As a result, the system has finite mass terms characterized by the renormalized m^* value, and the HOTI phase can survive in the presence of weak intersector forward scatterings.

[1] R. Jackiw and C. Rebbi, Solitons with fermion number $\frac{1}{2}$, Phys. Rev. D **13**, 3398 (1976).

[2] W. P. Su, J. R. Schrieffer, and A. J. Heeger, Soliton excitations in polyacetylene, Phys. Rev. B **22**, 2099 (1980).

[3] A. J. Heeger, S. Kivelson, J. R. Schrieffer, and W. P. Su, Solitons in conducting polymers, Rev. Mod. Phys. **60**, 781 (1988).

[4] Y. Hwang, J. Ahn, and B.-J. Yang, Fragile topology protected by inversion symmetry: Diagnosis, bulk-boundary correspondence, and Wilson loop, Phys. Rev. B **100**, 205126 (2019).

[5] W. P. Su and J. R. Schrieffer, Fractionally charged excitations in charge-density-wave systems with commensurability 3, Phys. Rev. Lett. **46**, 738 (1981).

[6] M. J. Rice and E. J. Mele, Elementary excitations of a linearly conjugated diatomic polymer, Phys. Rev. Lett. **49**, 1455 (1982).

[7] H. Watanabe and H. C. Po, Fractional corner charge of sodium chloride, Phys. Rev. X **11**, 041064 (2021).

[8] H. Wada, K. Naito, S. Ono, K. Shiozaki, and S. Murakami, General corner charge formulas in various tetrahedral and cubic space groups, Phys. Rev. B **109**, 085114 (2024).

[9] Y. Fang and J. Cano, Filling anomaly for general two- and three-dimensional C_4 symmetric lattices, Phys. Rev. B **103**, 165109 (2021).

[10] K. Naito, R. Takahashi, H. Watanabe, and S. Murakami, Fractional hinge and corner charges in various crystal shapes with cubic symmetry, Phys. Rev. B **105**, 045126 (2022).

[11] Y.-Q. Wang and J. E. Moore, Boundary edge networks induced by bulk topology, Phys. Rev. B **99**, 155102 (2019).

[12] X. Zhu, Tunable Majorana corner states in a two-dimensional second-order topological superconductor induced by magnetic fields, Phys. Rev. B **97**, 205134 (2018).

[13] H. Mu, G. Zhao, H. Zhang, and Z. Wang, Antiferromagnetic second-order topological insulator with fractional mass-kink, npj Comput. Mater. **8**, 82 (2022).

[14] S. Spurrier and N. R. Cooper, Kane-Mele with a twist: Quasicrystalline higher-order topological insulators with fractional mass kinks, Phys. Rev. Res. **2**, 033071 (2020).

[15] B. Liu, L. Xian, H. Mu, G. Zhao, Z. Liu, A. Rubio, and Z. F. Wang, Higher-order band topology in twisted moiré superlattice, Phys. Rev. Lett. **126**, 066401 (2021).

[16] K. Le Hur, S. Vishveshwara, and C. Bena, Double-gap superconducting proximity effect in armchair carbon nanotubes, Phys. Rev. B **77**, 041406(R) (2008).

[17] C.-H. Hsu, P. Stano, J. Klinovaja, and D. Loss, Antiferromagnetic nuclear spin helix and topological superconductivity in ^{13}C nanotubes, Phys. Rev. B **92**, 235435 (2015).

[18] J. Klinovaja, S. Gangadharaiah, and D. Loss, Electric-field-induced Majorana fermions in armchair carbon nanotubes, Phys. Rev. Lett. **108**, 196804 (2012).

[19] C.-H. Hsu, P. Stano, J. Klinovaja, and D. Loss, Majorana Kramers pairs in higher-order topological insulators, Phys. Rev. Lett. **121**, 196801 (2018).

[20] F. Zhang, C. L. Kane, and E. J. Mele, Topological mirror superconductivity, Phys. Rev. Lett. **111**, 056403 (2013).

[21] R. A. Santos, D. B. Gutman, and S. T. Carr, Interplay between intrinsic and emergent topological protection on interacting helical modes, Phys. Rev. B **99**, 075129 (2019).

[22] C.-H. Hsu, P. Stano, J. Klinovaja, and D. Loss, Helical liquids in semiconductors, Semicond. Sci. Technol. **36**, 123003 (2021).

[23] J. L. Lado, D. Guterding, P. Barone, R. Valentí, and V. Pardo, Quantum spin Hall effect in rutile-based oxide multilayers, Phys. Rev. B **94**, 235111 (2016).

[24] J. Henke, M. Kurttutan, J. Kruthoff, and J. van Wezel, Topological invariants of rotationally symmetric crystals, Phys. Rev. B **104**, L201110 (2021).

[25] B. Wang, Y.-C. Hung, X. Zhou, A. Bansil, and H. Lin, Higher-order topological phases hidden in quantum spin Hall insulators, Phys. Rev. B **108**, 245103 (2023).

[26] E. Prodan, Robustness of the spin-Chern number, Phys. Rev. B **80**, 125327 (2009).

[27] H. Shulman and E. Prodan, Robust extended states in a topological bulk model with even spin-Chern invariant, arXiv:1011.5456.

[28] F. Schindler, S. S. Tsirkin, T. Neupert, B. A. Bernevig, and B. J. Wieder, Topological zero-dimensional defect and flux states in three-dimensional insulators, Nat. Commun. **13**, 5791 (2022).

[29] N. Kainaris and S. T. Carr, Emergent topological properties in interacting one-dimensional systems with spin-orbit coupling, Phys. Rev. B **92**, 035139 (2015).

[30] R. A. Santos, D. B. Gutman, and S. T. Carr, Phase diagram of two interacting helical states, Phys. Rev. B **93**, 235436 (2016).

[31] J. Cuevas-Maraver, P. Kevrekidis, and F. Williams, *The sine-Gordon Model and its Applications: From Pendula and Josephson Junctions to Gravity and High-Energy Physics* (Springer, Berlin, 2014).

[32] A. M. T. A. O. Gogolin, A. A. Nersesyan, *Bosonization and Strongly Correlated Systems* (Cambridge University Press, Cambridge, 1998).

[33] T. Giamarchi, *Quantum Physics in One Dimension* (Oxford University Press, New York, 2003).

[34] C.-K. Chiu, J. C. Y. Teo, A. P. Schnyder, and S. Ryu, Classification of topological quantum matter with symmetries, Rev. Mod. Phys. **88**, 035005 (2016).

[35] N. Kainaris, R. A. Santos, D. B. Gutman, and S. T. Carr, Interaction induced topological protection in one-dimensional conductors, Fortschr. Phys. **65**, 1600054 (2017).

[36] H. Shiba and M. Ogata, Properties of one-dimensional strongly correlated electrons, Prog. Theor. Phys. Suppl. **108**, 265 (1992).

[37] T. Kimura, K. Kuroki, and H. Aoki, Generation of spin-polarized currents in Zeeman-split Tomonaga-Luttinger models, Phys. Rev. B **53**, 9572 (1996).

[38] A. V. Moroz, K. V. Samokhin, and C. H. W. Barnes, Theory of quasi-one-dimensional electron liquids with spin-orbit coupling, Phys. Rev. B **62**, 16900 (2000).

[39] A. V. Moroz, K. V. Samokhin, and C. H. W. Barnes, Spin-orbit coupling in interacting quasi-one-dimensional electron systems, Phys. Rev. Lett. **84**, 4164 (2000).

[40] C.-H. Hsu, P. Stano, Y. Sato, S. Matsuo, S. Tarucha, and D. Loss, Charge transport of a spin-orbit-coupled Luttinger liquid, Phys. Rev. B **100**, 195423 (2019).

[41] X.-L. Qi and S.-C. Zhang, Spin-charge separation in the quantum spin Hall state, Phys. Rev. Lett. **101**, 086802 (2008).

[42] M. Thakurathi, P. Simon, I. Mandal, J. Klinovaja, and D. Loss, Majorana Kramers pairs in Rashba double nanowires with interactions and disorder, Phys. Rev. B **97**, 045415 (2018).

[43] T. Meng and D. Loss, Helical nuclear spin order in two-subband quantum wires, Phys. Rev. B **87**, 235427 (2013).

[44] G. Shavit and Y. Oreg, Fractional conductance in strongly interacting 1d systems, Phys. Rev. Lett. **123**, 036803 (2019).

[45] B. Wang, Y.-C. Hung, X. Zhou, T. Ong, and H. Lin, Feature spectrum topology, arXiv:2310.14832.

[46] J. Liu, T. H. Hsieh, P. Wei, W. Duan, J. Moodera, and L. Fu, Spin-filtered edge states with an electrically tunable gap in a two-dimensional topological crystalline insulator, Nat. Mater. **13**, 178 (2014).

[47] X.-L. Qi, T. L. Hughes, and S.-C. Zhang, Fractional charge and quantized current in the quantum spin Hall state, Nat. Phys. **4**, 273 (2008).

[48] E. Miranda, Introduction to bosonization, Braz. J. Phys. **33**, (2003).

[49] C. L. Kane, R. Mukhopadhyay, and T. C. Lubensky, Fractional quantum Hall effect in an array of quantum wires, Phys. Rev. Lett. **88**, 036401 (2002).

[50] C.-H. Hsu, D. Loss, and J. Klinovaja, General scattering and electronic states in a quantum-wire network of moiré systems, Phys. Rev. B **108**, L121409 (2023).